

# Various pole figure measurement techniques with SmartLab, assisting thin film characterization

Katsuhiko Inaba\* and Shintaro Kobayashi\*\*

## 1. Introduction

A pole figure (PF) measurement is an X-ray diffraction (XRD) technique employed for the observation of textures in polycrystalline materials in the form of bulk ceramics, metal complex, thin films, etc, or the analysis of the orientation or domain configuration of epitaxial thin films<sup>(1)–(4)</sup>. A comprehensive explanation of pole figures can be found in the technical article “X-ray thin film measurement techniques” in the Rigaku Journal<sup>(1)</sup>. However, we often receive questions or requests for technical advice about PF measurements, especially for thin film samples. Users may wonder which of three PF measurement methods should be employed using a SmartLab system equipped with an in-plane axis and a 2D detector. This is the reason for this lecture note. Features of the three possible PF measurements will be reviewed to guide SmartLab users, studying thin film samples. Since a pole figure measurement using an in-plane axis is such a unique and useful technique, it merits a discussion of updated applications using this technique for modern functional materials.

## 2. Comparison of three PF measurement techniques

### 2.1. Short remarks about PF measurements

A pole figure measurement is a technique where the diffraction angle is fixed and the diffracted intensity is recorded by varying two geometrical parameters, such as the  $\alpha$  angle (tilt angle of the diffraction vector from the surface normal direction of a sample) and the  $\beta$  angle ( $\phi$  rotation angle of the diffraction vector around surface normal direction of a sample). These two parameters can be compared to the latitude and longitude of the Earth, respectively. In the case of thin film analysis, the  $\alpha$  angle is commonly referred to as the elevation angle of the diffraction vector from the surface of a sample, thus  $\alpha=0^\circ$  denotes the condition for in-plane diffraction measurements and  $\alpha=90^\circ$  denotes the condition for  $\theta$ - $2\theta$  measurements<sup>(1)</sup>. In this paper, the tilting angle of a diffraction vector from the direction of the sample surface normal is denoted as  $\psi$ .

In a PF measurement, the diffraction angle ( $2\theta_B$ ) is fixed. Therefore, the diffracted intensity distribution on the curved surface at a constant distance from the coordinate origin in the reciprocal space is measured.

On the other hand, in the case of reciprocal space map (RSM) measurements, the signal intensity distribution on a flat cross section plane passing through the coordinate origin is observed<sup>(1), (5)–(8)</sup>. Figure 1 shows the comparison between a pole figure measurement and the ordinary RSM measurement in a schematic diagram.

Since the diffraction angle is fixed in a PF measurement, this technique is insensitive to slight difference in diffraction angles, which should be measured in elastically-deformed epitaxial thin films constrained to substrates. For that purpose RSM measurement is effective. On the other hand, in order to discuss orientation relationships between epitaxial thin films and substrates, it is better to employ PF measurements. This is because, in the RSM measurement, the orientation relationship between substrates and epitaxial thin films should be predicted beforehand and the arrangement relation between the reciprocal lattice points of the substrate and the thin films will be discussed, so that unexpected orientation relationships between them are sometimes missed. For the case of analyses of epitaxial thin films with complex domains, more detailed analyses with combinations of measurements such as PF measurements, wide-range RSM measurements, in-plane RSM measurements and the like are to be performed, with the aid of reciprocal space simulation tools<sup>(4), (7), (8)</sup>.

### 2.2. Conventional PF measurements

With a SmartLab system for thin film samples, equipped with a  $\chi$  axis cradle, changing the  $\alpha$  and  $\beta$  angles can be done with motions of the  $\chi$  axis and  $\phi$  axis, respectively. For a Smartlab system without a  $\chi$  axis cradle, PF measurement can be performed by mounting

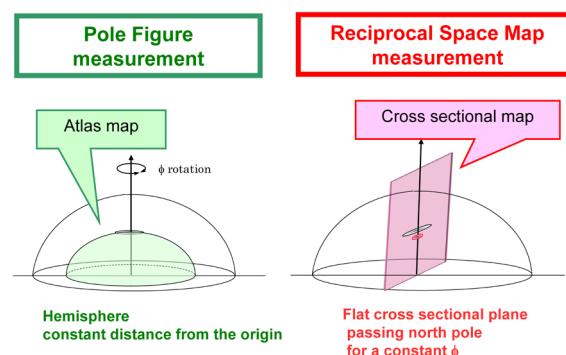


Fig. 1. Schematic illustration of pole figure measurement and reciprocal space map measurement.

\* X-ray Research Laboratory, Rigaku Corporation.

\*\* Application Laboratories, Rigaku Corporation.

an  $\alpha\beta$  attachment. A detailed explanation of the use of this attachment was previously provided in Ref. (1). Some important features of this measurement technique for comparison with other PF measurement techniques will be discussed in this lecture.

First of all, as mentioned above, the actual measurement can be performed by operating the  $\chi$  axis and  $\phi$  axis, and the movement of the goniometer is very simple.

In a PF measurement, the goniometer should keep the same conditions as for a  $\theta$ - $2\theta$  measurement with respect to the X-ray source and the detector. So, the  $2\theta_B$  angle is always equal to the  $2\theta$  angle, since the detector position is manipulated only by the  $2\theta$  angle. However, care must be taken in the way the sample is held, because it will be tilted with the motion of the  $\chi$  axis, even though the sample will be held horizontal when the  $\chi$  angle is  $0^\circ$ .

Further, to avoid the situation where the incident X-rays extend beyond from the surface of a sample during measurement, it is necessary to shape the incident X-rays to a point shape.

A common optical element to produce a point-shaped incident X-ray beam is a Schulz slit<sup>(1)</sup> or a collimator. Another candidate for this purpose is a CBO- $f$  unit<sup>(9), (10)</sup> to convert a line-shaped beam to a point-shaped beam, with which monochromated incident X-rays from a CBO unit can be employed for the measurements.

However, the exposed area of the sample surface is inevitably wide due to the projection of the incident X-rays at low incident angles, which means that diffracted signals are not practically accessible when the  $\chi$  is greater than  $70^\circ$ ; i.e., the  $\alpha < 20^\circ$  regions<sup>(1)</sup>.

### 2.3. PF measurements using a 2D detector

By using a 2D detector, distributed signals in a wide range of reciprocal space can be recorded<sup>(1), (7)</sup>. This feature allows wide-range RSM measurements to be performed in a short time. In those measurements, TDI scans are employed to cover a wide range in  $2\theta_B$  angles. On the other hands, PF measurements using a 2D detector are done with successive snapshot measurements with a fixed detector position and varying  $\phi$ <sup>(1)</sup>.

Figure 2 shows a snapshot image with a 2D detector for a polycrystalline ZnO thin film with a weak preferred orientation texture. Multiple reflections from the ZnO thin film can be seen as arcs in this image, showing wide distributions for these signals along the  $\alpha$  direction. The coverage along the  $\alpha$  direction is defined as a function of the  $2\theta_B$  angle for the center of the detector and the camera length (the distance from the center of the sample to the center of the detector) as a geometrical acceptance of the width of the 2D detector. The image in Fig. 2 was taken at a camera length of 150 mm, a  $2\theta$  angle of  $34^\circ$ , and a  $\chi$  angle of  $30^\circ$ , where the coverage range along the  $\alpha$  direction is approximately  $\pm 25^\circ$ . Therefore, it requires only a few positions of the  $\chi$  axis (for instance,  $\chi = 0^\circ, 30^\circ, 60^\circ$ ) to complete a PF measurement.

The angular range of  $25^\circ$  to  $40^\circ$  for  $2\theta_B$  was covered in the image in Fig. 2. Due to such wide  $2\theta_B$

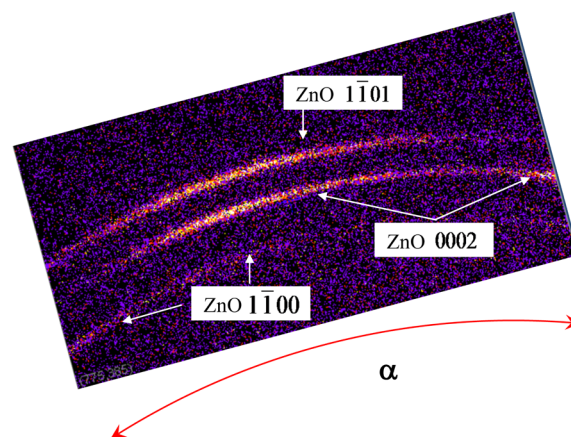


Fig. 2. 2D diffraction image of a polycrystalline ZnO thin film with a weak preferred orientation texture.

coverage, signals from three different reflections from the ZnO thin film are observed in the image, such as  $1\bar{1}00$  ( $2\theta_B = 31.8^\circ$  for  $\text{CuK}\alpha$ ),  $0002$  ( $2\theta_B = 34.4^\circ$ ), and  $1\bar{1}01$  ( $2\theta_B = 36.3^\circ$ ). PF measurements for these three reflections are finished in an extremely short time, for example 20 minutes with the measuring conditions found in these snapshots with an exposure time of several seconds and  $5^\circ$  step of the  $\phi$  axis.

Since the measurement is performed in 2D mode of the 2D detector, a point-shaped beam for the incident X-rays should be employed<sup>(1), (4), (6), (7)</sup>. Care must be taken in the way the sample is held, because it will be tilted with the motion of the  $\chi$  axis, even though the sample will be horizontal when the  $\chi$  angle is  $0^\circ$ . Also, the exposed area of the sample surface is inevitably wide due to the projection of the incident X-rays at low incident angles, which means that diffracted signals are not practically accessible when the  $\chi$ -angle is greater than  $70^\circ$ ; i.e.,  $\alpha < 20^\circ$  region. The latter two issues are the same as for the conventional PF measurements explained in Sect. 2.2.

During a PF measurement, the detector position is controlled with the  $2\theta$  axis, so that the center of the detector is moved to the position where  $2\theta = 2\theta_B$  as input in the operation software, maintaining a  $\theta$ - $2\theta$  configuration. Since this measurement is performed not with TDI scans, but by collecting successive snapshots, the incident angle ( $\theta$ ) to the sample surface is kept constant during the measurement. This situation implies that only pixels aligned in the arc along the  $\alpha$  direction passing through the center pixel of the detector will satisfy the  $\theta$ - $2\theta$  configuration. Other pixels will collect signals under an asymmetric configuration with respect to the incident X-rays and the diffracted X-rays. Due to this asymmetry, data collection at  $\alpha = 90^\circ$  is possible only for diffraction signals that coincide with the input  $2\theta_B$  value. For data collection around  $\alpha = 90^\circ$  for diffraction signals in which the  $2\theta_B$  value deviates from the input value, additional measurements with the condition satisfying the symmetric configuration are required.

### 2.4. PF measurements using an in-plane axis

The  $\chi$  axis for sample tilting is not required for this measurement; instead, the in-plane axis ( $2\theta\chi$  axis) is used. This measurement technique is called “PF measurement using in-plane axis”, sometimes abbreviated to “in-plane PF”. Please note, however, that the in-plane diffraction technique itself cannot be used to perform PF measurements. Figure 3 schematically illustrates the goniometer motion during this measurement.

You may wonder why PF measurements can be performed without equipping the system with a tilting axis on the system. In order to collect signals in the direction diagonal to the sample surface normal, a sophisticated technique is implemented in the system to collect the signal distributions along the Debye rings, without requiring a tilting axis.

The position of the detector in 0D mode is manipulated by the  $2\theta$  and  $2\theta\chi$  axis. The combination of  $2\theta$  and  $2\theta\chi$  angles can be converted to a combination of  $2\theta_B$  and  $\alpha$  angles. The PF measurement is performed in this scheme without manipulation of the  $\chi$  axis so that  $\chi$  can be fixed at  $0^\circ$  which means that the sample can be kept horizontal during PF measurements. An application example of this technique will be seen in Sect. 3.

As was the case with the previous two techniques, a

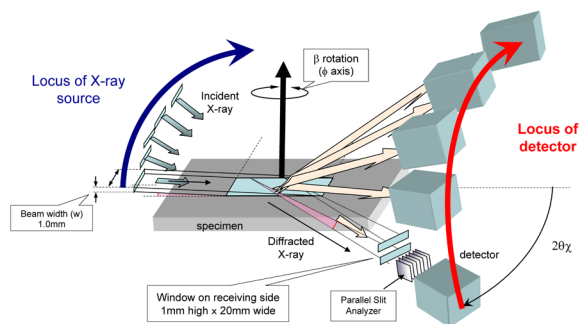


**Fig. 3.** Goniometer motion for pole figure measurement using in-plane axis.

point-shaped beam can be used for PF measurements using the in-plane axis. However, a line-shaped beam can also be employed in this technique, because the sample will not be tilted. Instead, it is recommended that in-plane PSC optics is used in the incident optics. As can be easily understood, the range of  $\alpha$  from  $0^\circ$  to  $90^\circ$  can be continuously covered with this technique, resulting in data collection of an entire hemisphere of reciprocal space.

To measure PFs over  $10^\circ$  in  $\alpha$ , an incident beam width of 1 mm is reasonable. Use a narrow width-limiting-slit (for example, 0.1 mm in “IS”) in the incident optics for PF measurements that cover the  $\alpha$  angle range from  $0^\circ$  to suppress the effect of the extension of the incident X-rays beyond the surface of the sample.

The  $\beta$  angle in this measurement is controlled by a complicated set of axis operations as involving the  $\phi$ ,  $\omega$ ,  $2\theta$ , and  $2\theta\chi$  axes at the same time. Therefore, even though the measurement is a simple  $\alpha$  scan, it involves complicated operation of the four axes mentioned above. Users of a SmartLab system should not worry about this, though, because you only need to input parameters in the operation software windows, such as the  $2\theta_B$  angle of the diffraction signal to be measured, a range and step size for the  $\alpha$  angle, and a step size and scan speed for the  $\beta$  angle. In addition, in “3D Explore”, a display/analysis program for PF data provided by Rigaku, many useful functions are implemented, such as a function to extract intensity profiles along the  $\alpha$  and  $\beta$  axes from the data obtained, a function to display intensity profiles with averaging over a designed width specified by the user, a function to export text data for profiles, etc.

Features of the three PF measurement methods shown above are summarized in Table 1.

### 3. Application to functional materials

In this section, results of analysis of functional materials via pole figure measurements using the in-plane axis will be shown.

**Table 1.** Feature summary of three PF measurement techniques.

	Conventional PF measurements	PF measurements using 2D detector	PF measurements using in-plane axis
Operation of goniometer	<ul style="list-style-type: none"> <li><math>\theta</math>-<math>2\theta</math> configuration</li> <li>Manipulated with <math>\chi</math> and <math>\phi</math> axis</li> </ul>	<ul style="list-style-type: none"> <li><math>\theta</math>-<math>2\theta</math> configuration</li> <li>Snapshots with <math>\phi</math> steps at various <math>\chi</math> positions</li> </ul>	<ul style="list-style-type: none"> <li><math>\phi</math> scans with step motions for <math>\omega</math>, <math>2\theta</math>, and <math>2\theta\chi</math> axes (<math>\chi</math> axis if fixed at <math>0^\circ</math>)</li> </ul>
Optics	<ul style="list-style-type: none"> <li>Point-shaped beam required</li> </ul>	<ul style="list-style-type: none"> <li>Point-shaped beam required</li> </ul>	<ul style="list-style-type: none"> <li>Line-shaped beam (Optics for in-plane measurement) Or Point-shaped beam</li> </ul>
Features	<ul style="list-style-type: none"> <li>Popular and simple operation</li> <li>Care for sample holding required because of sample tilting.</li> <li>Practically inaccessible in the range below <math>20^\circ</math> for <math>\alpha</math></li> </ul>	<ul style="list-style-type: none"> <li>Wide range of <math>\alpha</math> direction can be covered with 2D detector</li> <li>Possible to collect signals from multiple indices simultaneously</li> <li>Care for sample holding required because of sample tilting</li> <li>Practically inaccessible in the range below <math>20^\circ</math> for <math>\alpha</math></li> </ul>	<ul style="list-style-type: none"> <li>Possible to keep sample in horizontal plane</li> <li>Possible to cover for <math>\alpha</math> from <math>0^\circ</math> to <math>90^\circ</math></li> <li>In-plane axis required</li> </ul>

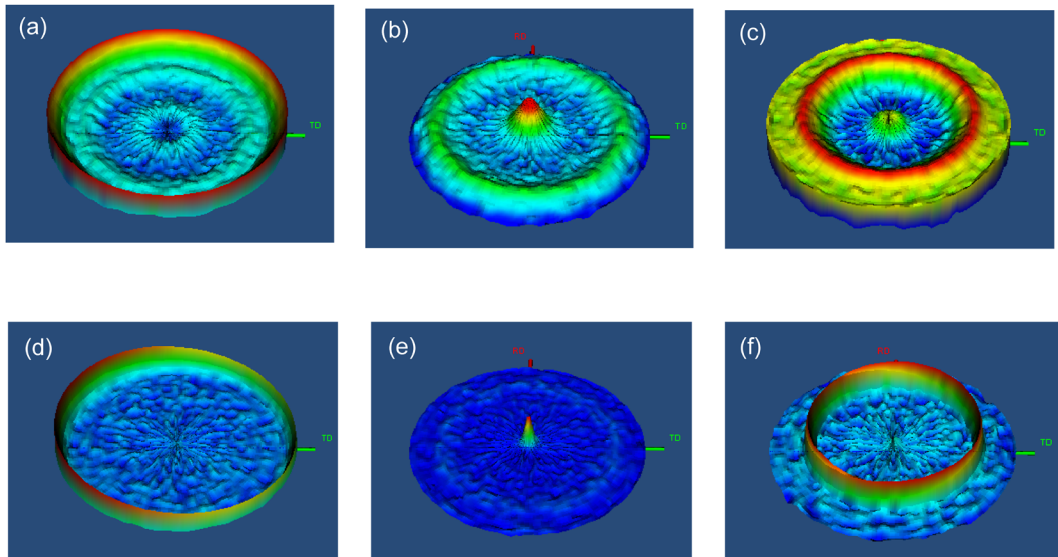


**Fig. 4.** Data of pole figures using in-plane axis.  
 (a) to (c): ZnO thin film with weak texture. (a):  $1\bar{1}00$  reflection, (b): 0002 reflection, (c):  $1\bar{1}01$  reflection.  
 (d) to (f): ZnO thin film with strong texture. (d):  $1\bar{1}00$  reflection, (e): 0002 reflection, (f):  $1\bar{1}01$  reflection.  
 Intensities are shown in log scale.

### 3.1. ZnO transparent conductive oxide thin films

ZnO transparent conductive oxide (TCO) thin films are widely used in various industrial fields.

Our group has been investigating the characteristics of transporting properties and crystallographic orientation distributions in Al-doped or Ga-doped ZnO thin films on glass substrates grown by sputtering methods. Explanations of growth methods and growth conditions can be found in Ref. (11)–(14) together with the concept of the technique to control the preferred orientation texture for these films.

A strong preferred orientation texture was greatly promoted, resulting in remarkable improvements in electric transport properties in ZnO films by the introduction of an interface layer on glass substrates to tailor the texture and surface morphology of these films. Data shown in Fig. 4 are the results of PF measurements using the in-plane axis for 500 nm-thick ZnO films. Figure 4 (a)–(c) are PF data for a ZnO film without the introduction of an interface layer, for the  $1\bar{1}00$ , 0002, and  $1\bar{1}01$  reflections, respectively. Figure 4(d)–(f) are PF data for a ZnO film in which an interface layer was introduced at the initial stage of film growth, again for the  $1\bar{1}00$ , 0002, and  $1\bar{1}01$  reflections, respectively. The outer rims of the disk-like images in these figures correspond to signals collected at  $\alpha=0^\circ$  (observing signals from lattice planes perpendicular to the sample surface) and the centers of the disk-like images correspond to signals collected at  $\alpha=90^\circ$  (observing signals from lattice planes parallel to the sample surface). Data are displayed in 3D topographic modes, and with the intensities shown in log scale.

As can be readily seen, poles of 0002 reflections in Fig. 4(b) and (e) are positioned at the center of the data, implying that these films have a (0001) orientation texture as a major component. Typical uniaxial

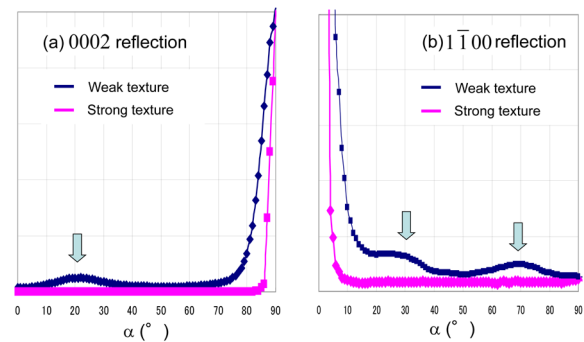


**Fig. 5.**  $\alpha$ -scan profiles. (a) 0002 reflection, (b)  $1\bar{1}00$  reflection.

textures isotropic within surface planes (random in azimuthal distribution) are also expected since intensity distributions along the circumferential directions of the outer rims are constant. However, the pole of the 0002 reflection observed in Fig. 4(e) is sharper than the one in Fig. 4(b). This fact indicates that the ZnO film introduced with an interface layer has a strong preferred orientation texture. In Fig. 4(b), a ring of faint maxima (poles) close to the outer rim can be observed, implying the possible co-existence of another orientation texture other than a (0001) orientation texture. It was found that this maximum is positioned at  $\alpha=21^\circ$  ( $\psi=69^\circ$ ) from the profile analysis of  $\alpha$ -scans shown in Fig. 5(a), extracted from data in Fig. 4(b) and (e).

Next, let us examine data for the  $1\bar{1}00$  reflections shown in Fig. 4(a) and (d). Since  $\{1\bar{1}00\}$  lattice planes are perpendicular to the  $c$ -plane of ZnO, diffraction signals of  $1\bar{1}00$  reflections from ZnO films with a (0001) orientation texture will show their poles (maxima) at  $\alpha=0^\circ$ ; i.e., observed as rings at the outer rims. This prediction is consistent with the data shown in Fig. 4(a) and (d). It should be emphasized that this

analysis is enabled with the “pole figure measurements using in-plane axis” technique, where data collection is possible in the range from  $\alpha=0^\circ$  to  $\alpha=90^\circ$ , continuously.

Here again, the existence of two faint rings of maxima besides the outer rims observed in Fig. 4(a) suggests the possible co-existence of other orientation texture(s) different from a (0001) orientation texture. It was confirmed that these maxima are positioned at  $\alpha=28^\circ$  ( $\psi=62^\circ$ ) and  $\alpha=69^\circ$  ( $\psi=21^\circ$ ) from the profile analysis of  $\alpha$  scans shown in Fig. 5(b), extracted from data in Fig. 4(a) and (d).

Rings of maxima were observed at the inner parts for the data in Fig. 4(c) and (f). These rings are positioned at  $\alpha=28^\circ$  ( $\psi=62^\circ$ ). This observation is reasonably explained from the fact that the direction of the normal of  $\{1\bar{1}01\}$  lattice planes of ZnO is tilted from the  $c$  axis of ZnO by  $61.6^\circ$ .

The ring observed in Fig. 4(c) is wider than the one in Fig. 4(f). This is also indicative of the nature of weak preferred orientation texture for ZnO film without the introduction of an interfacial layer at the initial growth stage. The appearance of weak rings of maxima in Fig. 4(c) also suggests the possible co-existence of other orientation texture(s) different from a (0001) orientation texture.

In the next step, a more detailed analysis of the preferred orientation texture other than the major (0001) orientation texture in the weakly-textured ZnO film was performed. From the discussion above for the data shown in Fig. 5(a), it is expected that the  $c$  axis of ZnO for the second component of the preferred orientation texture is tilted from the surface normal direction by ca.  $69^\circ$ , as found in Fig. 5(a). One possibility for the lattice planes of low order indices that intersect by  $69^\circ$  relative to  $c$  plane is a  $\{3\bar{3}02\}$  lattice plane. The  $\{3\bar{3}02\}$  lattice plane of ZnO runs almost parallel to a plane of rigid  $\text{ZnO}_4$  tetrahedra in the wurtzite lattice, thus is expected to be an energetically stable plane. A model analysis of PF patterns for ZnO film having a hypothetical  $\{3\bar{3}02\}$  preferred orientation texture was performed. At first, the  $\alpha$  and  $\beta$  angles for 0002 reflections and  $1\bar{1}00$  reflections for a single crystal ZnO with the orientation where one of its  $\{3\bar{3}02\}$  planes is parallel to the sample surface were calculated. Secondly, PF patterns for ZnO film of a  $(3\bar{3}02)$  preferred orientation texture were simulated by assuming that PF patterns will appear as rings due to random orientation within the surface plane. The result is shown in Fig. 6. A green ring corresponds to 0002 reflections and yellow rings are for  $1\bar{1}00$  reflections. It should be noted that  $1\bar{1}00$  reflections appear as two rings positioned at  $\alpha=28.1^\circ$  ( $\psi=61.9^\circ$ ) and  $\alpha=70.2^\circ$  ( $\psi=19.8^\circ$ ). Since the result of this simulation agrees well with the observation shown in Fig. 5(b), it is a reasonable assumption that the ZnO film without the introduction of an interfacial layer contains two preferred orientation textures, such as a (0001) texture as a major texture, and a  $(3\bar{3}02)$  texture as a secondary texture. In order to verify this estimation, a  $\theta$ - $2\theta$  scan in

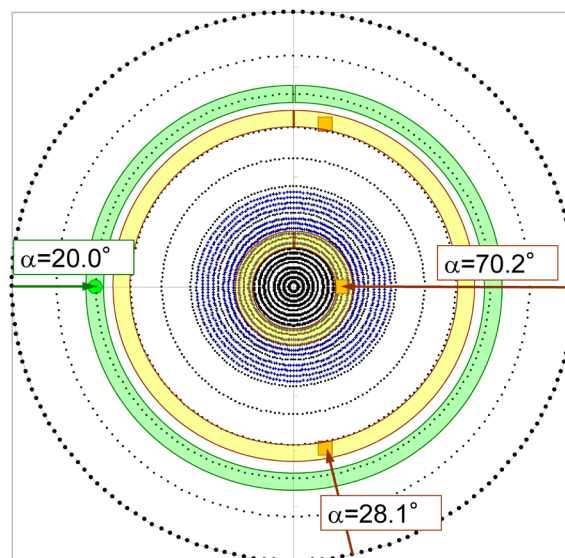


Fig. 6. A result of PF simulation for  $(3\bar{3}02)$ -textured ZnO (Green band for 0002 reflection, yellow band for  $1\bar{1}00$  reflection).

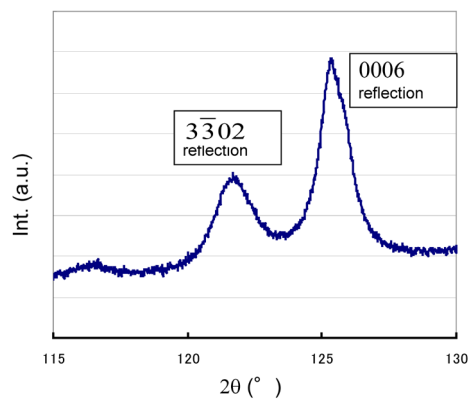


Fig. 7. A  $\theta$ - $2\theta$  scan profile for ZnO thin film with weak texture.

the higher  $2\theta$  range was performed. The result is shown in Fig. 7, where the  $3\bar{3}02$  reflection was observed in the  $\theta$ - $2\theta$  scan profile close to the 0006 reflection.

### 3.2. PFs of single crystalline materials

Pole figure measurement techniques can be applied not only to polycrystalline materials, but also to single crystalline materials, such as bulk single crystalline blocks or single crystal wafers. For example, it is common to use special equipment to perform the Laue method to determine the orientation of a block of single crystal materials. PF analysis using a SmartLab system will easily satisfy this purpose. In this approach, it is better to target the crystallographic axis with higher symmetry to simplify the analysis; for example,  $000l$  reflections for a material with hexagonal symmetry, or  $00l$  reflections for those with tetragonal symmetry.

Some readers may have experience characterizing crystalline quality of single crystal materials using a conventional PF measurement technique, and

consequently obtained a wide-spread pole from a sample. With PFs using the in-plane axis, sharp spots can be obtained for single crystalline materials. Figure 8 shows PF data for the 113 reflection from a single crystal Si (001) wafer collected by PF using the in-plane axis. The angular range of the data shown in Fig. 8 is  $\pm 4^\circ$  for both the  $\alpha$  and  $\beta$  axes, and the measurement was done with a small step width of  $0.1^\circ$ .

Figure 9(a) shows a picture of a ZnO single crystal grown by the hydrothermal synthesis method. The size of this crystal is about 5 mm in the horizontal direction in the figure. This crystal showed well-developed facet planes, not only  $c$  planes and  $m$  planes, but also pyramidal planes shown with red arrows in the figure. The index of these pyramidal

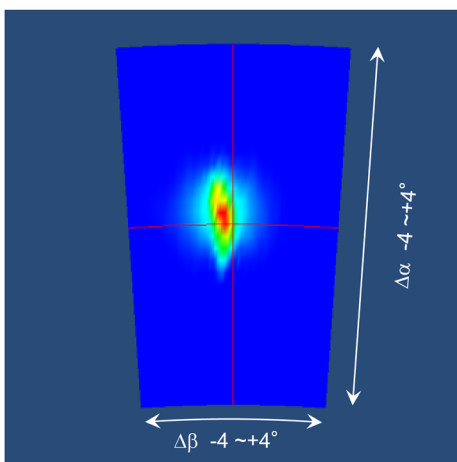


**Fig. 8.** A close-up view of PF data using in-plane axis for a Si (001) single crystalline wafer. Index of the reflection is 113, range for  $\alpha$  and  $\beta$  is  $\pm 4^\circ$ . Intensity is shown in log scale.

facet planes was investigated. In this approach, the sample was mounted on a sample plate without glue so that corresponding pyramidal planes were placed downward horizontally, as shown in Fig. 9(b). As a first step, a simple  $\theta-2\theta$  scan was performed and a  $1\bar{1}01$  reflection was detected. This result indicates that these pyramidal facet planes are  $\{1\bar{1}01\}$  planes. For further confirmation, PF measurements of the  $1\bar{1}01$  reflection were performed. The result is shown in Fig. 9(c). One of the poles can be seen at the center of the figure ( $\alpha=90^\circ$ ), and this result is consistent with the preliminary result. However, the distribution pattern of other poles seen in the figure becomes very complicated, due the direction of sample mounting. If this sample was mounted on a sample plate, where a top or bottom plane in Fig. 9(a) was parallel to a sample plate, a clear six-fold symmetry of  $1\bar{1}01$  reflection poles would be recognized, since a top or bottom plane in Fig. 9(a) is the  $c$  plane of the hexagonal wurtzite structure of ZnO. Similar situations may happen for the case of analysis of a single crystalline sample of unknown orientation. Therefore, a manipulating function in the displaying software to rotate data in the aspect of the  $\alpha$  axis or  $\beta$  axis by specified values is very useful. This functionality is implemented in the aforementioned program, “3D Explore”. Next, an analytical example utilizing this functionality is shown.

The sample is a ZnTe thin film epitaxially grown on a Si (110) substrate<sup>(16)</sup>. Figure 10(a) shows PF data for the 111 reflection of ZnTe. Since the appearance of these poles was so complicated, the possibility of domain formation caused by twinning on (111) in ZnTe was supposed. Domains caused by twinning on (111) are easily analyzed in PF data where the normal direction of (111) is placed at the center of the data. The data

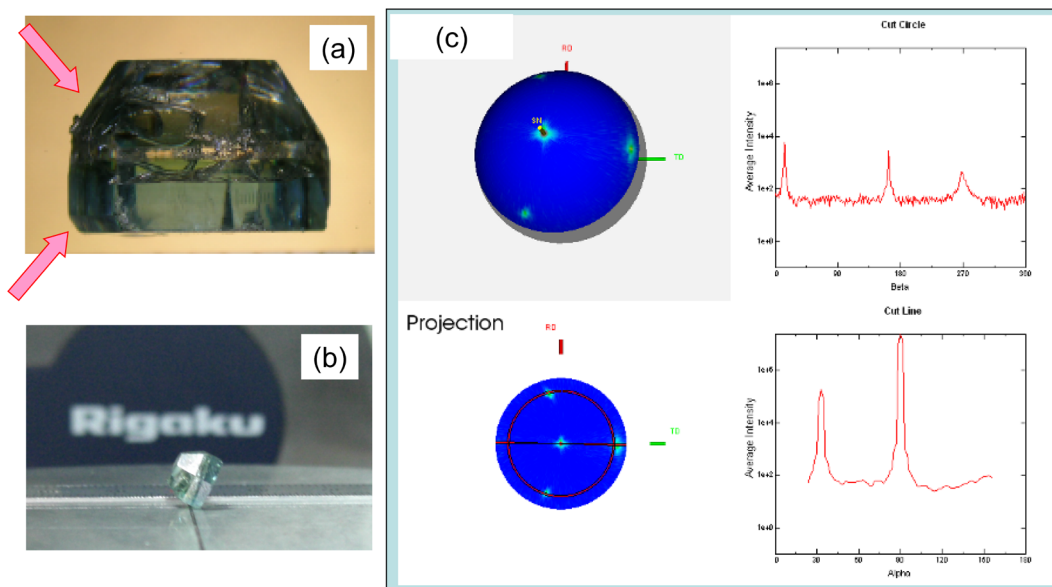


**Fig. 9.** (a) A picture of a ZnO single crystal grown by hydrothermal method. (b) A picture of a ZnO sample mounted on sample stage of SmartLab system (the sample, mounted on a pyramidal facet plane shown by a red arrow in Fig. 9(a) is lying in a horizontal plane. (c) Pole figure data.

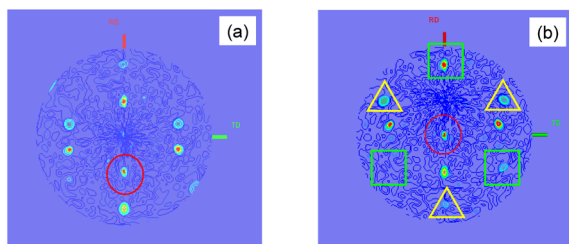


**Fig. 10.** (a) PF data for 111 reflection of ZnTe epitaxial film on Si (110) substrate. (b) PF data after rotation (see text details).

after manipulation, in which the pole marked with a red circle in Fig. 10(a) comes to the center of the image, is shown in Fig. 10(b) using a function in the program “3D Explore”.

In this figure, six poles appear at around  $\alpha=20^\circ$  with  $60^\circ$  intervals in the  $\beta$ -axis direction, thus showing six-fold symmetry. Considering a fact that each  $\{111\}$  plane of ZnTe of cubic symmetry intersects with each other by  $70.5^\circ$ , appearance of poles at  $\alpha=20^\circ$  is quite reasonable, but intervals in the  $\beta$ -axis direction must be  $120^\circ$  for a single crystal ZnTe film, since the  $[111]$  axis of cubic ZnTe should show three-fold symmetry. Therefore, these six poles at  $\alpha=20^\circ$  must be the contribution from two single crystal domains correlated to each other by  $60^\circ$  (or  $180^\circ$ ) rotation around the  $[111]$  axis. Poles originating from the same domain are marked by yellow triangles or green squares in Fig. 10(b). This correlation of two identical domains is often caused by the twinning. For the present case, the twinning is presumed to happen during the growth stage of ZnTe film.

#### 4. Conclusion

Various pole figure measurement techniques that can be performed with SmartLab systems were described together with application examples. Pole figure measurement techniques can be applied not only for texture analysis of polycrystalline bulk materials or thin films, but also for orientation analysis of single crystal materials, for analysis of coexisting preferred orientation textures or complicated domain configurations<sup>(4)</sup>, etc. It is expected that X-ray diffraction techniques will widely contribute to researches on various functional materials

in the future.

#### Acknowledgements

We would like to offer great thanks to Prof. Dr. T. Yamamoto, the Head of the Materials Design Center, Research Institute of Kochi University of Technology, Japan, and Dr. Jun-ichi Nomoto in Advanced Coating Technology Research Center, National Institute of Advanced Industrial Science and Technology, Japan for ZnO films shown in Sect.3.1.

#### References

- (1) K. Nagao and E. Kagami: *Rigaku Journal (English version)*, **27** (2011), No. 2, 6–14.
- (2) M. Birkholz: “*Thin Film Analysis by X-Ray Scattering*,” Wiley-VCH Verlag GmbH & Co., (2006).
- (3) O. Engler and V. Randle: “*Introduction to Texture Analysis—Macrotecture, Microtexture, and Orientation Mapping—*,” CRC Press (2010).
- (4) K. Inaba, S. Kobayashi, K. Uehara, A. Okada, S. L. Reddy and T. Endo: *Adv. Mater. Phys. Chem.*, **3** (2013), 72–89 (Open Access). <http://dx.doi.org/10.4236/amc.2013.31A010>
- (5) T. Konya: *Rigaku Journal (English version)*, **25** (2009), No. 2, 1–8.
- (6) S. Kobayashi and K. Inaba: *Rigaku Journal (English version)*, **28**, (2012), No. 1, 8–13.
- (7) S. Kobayashi and K. Inaba: *Rigaku Journal (English version)*, **32** (2016), No. 2, 1–5.
- (8) K. Inaba: *Rigaku Journal (English version)*, **33** (2017), No. 1, 10–14.
- (9) K. Nagao: *Rigaku Journal (English version)*, **27** (2011), No. 2, 15–21.
- (10) T. Osakabe: *Rigaku Journal (English version)*, **33** (2017), No. 1, 15–19.
- (11) J. Nomoto, K. Inaba, S. Kobayashi, T. Watanabe, H. Makino and T. Yamamoto: *Materials*, **10** (2017), 916-1-918-18 (Open Access). <http://www.mdpi.com/1996-1944/10/8/916>
- (12) J. Nomoto, K. Inaba, S. Kobayashi, H. Makino and T. Yamamoto: *Jour. Cryst. Growth*, **468** (2017), 645–649.
- (13) J. Nomoto, K. Inaba, M. Osada, S. Kobayashi, H. Makino and T. Yamamoto: *Jour. Appl. Phys.*, **120** (2016), 125302-1-125302-11.
- (14) J. Nomoto, H. Makino and T. Yamamoto: *Nanoscale Res. Lett.*, **11** (2016), 320-1-320-8 (Open Access). <https://nanoscalereslett.springeropen.com/articles/10.1186/s11671-016-1535-1>
- (15) K. Inaba: *The 4th Asian Conf. on Crystal Growth and Crystal Technology (CGCT-4)*, at Sendai, Japan, (2008), N\_24AM1\_II\_8C\_3.
- (16) M. Kobayashi, Y. Kumagai, T. Baba and S. Imada: *Phys. Stat. Sol.,-(c)*, **9** (2012), 1748–1751.